

Article

Experimental Kinetics Study on Diethyl Carbonate Oxidation

Sean P. Cooper , Claire M. Grégoire , Yousef M. Almarzooq, Eric L. Petersen and Olivier Mathieu 

J. Mike Walker '66 Department of Mechanical Engineering, Texas A&M University,
College Station, TX 77843, USA

* Correspondence: olivier.mathieu@tamu.edu

Abstract: Diethyl carbonate (DEC) is a common component of the liquid electrolyte in lithium ion batteries (LIBs). As such, understanding DEC combustion chemistry is imperative to improving chemical kinetic modeling of LIB fires. To this end, a comprehensive experimental study was conducted to collect ignition delay times, CO time histories, and laminar flame speeds during DEC combustion. Ignition delay times were collected using a heated shock tube at real fuel–air conditions for three equivalence ratios ($\phi = 0.5, 1.0, \text{ and } 2.0$) near atmospheric pressure and for temperatures between 1182 and 1406 K. Another shock tube was used to collect CO time histories using a laser absorption diagnostic. These experiments were conducted for the same equivalence ratios, but highly diluted in argon and helium (79.25% Ar + 20% He) at an average pressure of 1.27 atm and a temperature range of 1236–1669 K. Finally, a heated constant-volume vessel was used to collect laminar flame speeds of DEC at an initial temperature and pressure of 403 K and 1 atm, respectively, for equivalence ratios between 0.79 and 1.38. The results are compared with different mechanisms from the literature. Good agreement is seen for the ignition delay time and flame speed measurements. However, significant deviations are observed for the CO time histories. A detailed discussion of the chemical kinetics is presented to elucidate the important reactions and direct future modeling efforts.

Keywords: diethyl carbonate; shock tube; ignition delay time; laser absorption; laminar flame speed



Citation: Cooper, S.P.; Grégoire, C.M.; Almarzooq, Y.M.; Petersen, E.L.; Mathieu, O. Experimental Kinetics Study on Diethyl Carbonate Oxidation. *Fuels* **2023**, *4*, 243–260. <https://doi.org/10.3390/fuels4020015>

Academic Editor: Elna Heimdal Nilsson

Received: 20 February 2023

Revised: 6 April 2023

Accepted: 18 May 2023

Published: 1 June 2023



Copyright: © 2023 by the authors. Licensee MDPI, Basel, Switzerland. This article is an open access article distributed under the terms and conditions of the Creative Commons Attribution (CC BY) license (<https://creativecommons.org/licenses/by/4.0/>).

1. Introduction

Lithium ion battery (LIB) fires are a considerable challenge for designers, as energy work is focused on increasing the energy density of battery systems to achieve society's electrification goals as well as improving electronics' battery life [1]. These fires are linked to the flammability of the electrolyte and pose not only a significant safety hazard due to the heat [2], but also the harmful chemicals that can be released during combustion [3]. Therefore, it is imperative to characterize the fundamental chemistry behind the electrolyte's flammability so strategies to prevent igniting batteries can be designed.

LIBs utilize an electrolyte mixture as a medium to exchange ions from one pole of the capacitor to another. For LIBs in particular, the electrolyte medium allows for the movement of lithium ions between the electrodes, making them continually rechargeable. This electrolyte medium consists of many different compounds, but they mainly comprise both linear and cyclic carbonates [4]. One of these common solvents is diethyl carbonate (DEC), a symmetric ester of carbonic acid and ethanol taking the form shown in Figure 1. Additionally, the chemical kinetics of DEC combustion are not only important to LIBs from a process safety perspective, but also from a transportation and propulsion perspective. Specifically, DEC is a candidate as an oxygenated additive in diesel fuel due to its availability, bio-derived nature, and reduction of CO₂ and particulate emissions [5–7].

As such, several recent studies have investigated the chemical kinetics of DEC combustion both experimentally and numerically. Nakamura et al. [8] conducted the first comprehensive kinetics study, producing ignition delay times (IDT) from a rapid compression machine (RCM) and a shock tube (ST), speciation from a jet-stirred reactor (JSR), as well as ab initio calculations for target ROO• isomerization rate constants. Conditions

investigated ranged in temperatures from 500 to 1300 K and at pressures of 10 and 30 bar for fuel-lean, stoichiometric, and fuel-rich mixtures. The resulting mechanism presented therein well-reproduced the IDT data and most of the speciation data. However, a significant under-prediction of at least 40% was shown for ethanol and ethylene, both formed via two of the most important reactions to DEC decomposition:

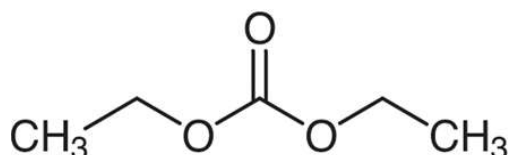
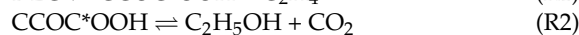


Figure 1. Molecular structure of diethyl carbonate (DEC).

Later, Shahla et al. [9] further investigated DEC combustion in a JSR, but at near atmospheric pressure and also presented laminar flame speed (LFS) data for DEC at an initial temperature of 393 K for pressures between 1 and 3 atm. This time, ethanol production was significantly overestimated by the model presented therein, while ethylene formation was well-predicted. The LFS data were well-reproduced by the model, but the number of data were limited, particularly at 1 and 3 atm, due to reported instability issues. Sun et al. [10] then measured speciation during DEC pyrolysis and combustion in a flow reactor for pressures up to 1 atm and presented rate coefficients for the pressure-dependent unimolecular decomposition of DEC using RRKM/master equation calculations. Sun et al. used these rate calculations to modify the Nakamura et al. [8] model, which significantly helped with reproducing the pyrolysis data, but issues remained for the oxidation data, particularly for ethanol, ethylene, and propane. The thermal unimolecular decomposition of DEC was investigated experimentally by AlAbbad et al. [11] in a shock tube, complemented by ab initio calculations. Excellent agreement with the measurements was found with the earlier study of Herzler et al. [12].

More recently, Sela et al. [13] utilized a single-pulse shock tube and a flow reactor to measure CO_2 , C_2H_4 , and $\text{C}_2\text{H}_5\text{OH}$ at temperatures between 663 and 1203 K at 1 and 2 bar. Additional ab initio calculations were performed, and the resulting rate coefficients were used to update the Sun et al. [10] mechanism. The resulting model well-reproduced the flow-reactor data and the DEC, ethanol, and ethylene shock-tube results. However, significant over-prediction is shown for the CO_2 shock-tube results. Even more recently, Kanayama et al. [14] and Takahashi et al. [15] released a comprehensive, two-part study on carbonate ester oxidation and pyrolysis in a micro-flow reactor with a controlled temperature profile at atmospheric pressure and temperatures between 700 and 1300 K. Kanayama et al. focused on ethyl methyl carbonate (EMC), while Takahashi et al. concentrated on dimethyl carbonate (DMC) and DEC and provided a good review of the literature for both. That is, Kanayama et al. thoroughly described the current state of affairs for DMC and DEC, introduced some new data in this area, and utilized the chemistry from these molecules to develop the first mechanism for EMC oxidation and pyrolysis. The resulting mechanism utilizes an updated Nakamura et al. model, taking advantage of reaction rate updates from Sun et al. [10] and Sela et al. [13]. While some progress has been made to improve modeling efforts for the combustion of carbonates, work remains for DEC combustion in particular. Specifically, additional IDT, LFS, and laser absorption data are needed to develop and validate chemical kinetics mechanisms.

To this end, the goal of this project is to develop a mechanism that can accurately predict thermal runaway in battery systems. To achieve this goal, a comprehensive study of the combustion properties of an average thermal-runaway gas (TRG), consisting of propane, ethane, ethylene, methane, hydrogen, carbon monoxide, and carbon dioxide, was conducted by Mathieu et al. [16], collecting IDT and H_2O time histories in a shock

tube and LFS in a constant-volume vessel. This review showed that the NUIGMech 1.1 mechanism [17] performs the best at reproducing TRG combustion, leading to it being the choice for base chemistry for the mechanism. Next, the fundamental chemistry of the pyrolysis of three common electrolytes, DMC, DEC, and EMC, was investigated by Grégoire et al. [18] using a shock tube to measure CO time histories near atmospheric pressure over a temperature range of 1230–2375 K. The Takahashi et al. [15] model was used for the DMC, DEC, and EMC submechanisms, with updates to the DMC submechanism using the work from Atherley et al. [19] and significant updates to the DEC submechanism using theoretically derived rates from Sela et al. [13] as well as updates to several initial decomposition reactions. Additionally, updates were made to the ethanol submechanism due to its rapid formation during DEC pyrolysis. The resulting mechanism (referred to here as the TAMU mechanism) well-reproduces the CO time histories presented therein, and does particularly well for the DEC results.

However, it is noted that significant issues remain with the base alcohol chemistry from the NUIGMech 1.1, contributing to poor EMC prediction. Mathieu et al. [20] also investigated bis(2,2,2trifluoroethyl)carbonate (DtFEC), a fluorinated carbonate with similar molecular structure to DEC. This study again collected IDT, LFS, and CO time histories, but for the combustion of H₂ and CH₄ with DtFEC as additive. A DtFEC submechanism was added to the TAMU mechanism, allowing for the comparison of DtFEC with DEC as a potential partial replacement for DEC in the electrolyte to minimize the LIB's reactivity. Therefore, a similar set of experiments is required and was performed in this study to accurately model DEC combustion at similar conditions. To this end, IDT and CO time histories were collected in a shock tube for combustion of DEC at fuel-lean, stoichiometric, and fuel-rich conditions near atmospheric pressure for temperatures between 1182 and 1669 K. Additionally, LFS data were measured using spherically expanding flames in a constant-volume vessel at initial conditions of 403 K and 1 atm. The data are compared with the TAMU mechanism as well as others from the literature, and a detailed discussion of the resulting chemistry is presented.

2. Experimental Methods

Low- and high-pressure shock-tube facilities were utilized to collect CO time histories and ignition delay time data, respectively. Additionally, a heated, constant-volume reactor was utilized to measure laminar flame speeds at various equivalence ratios. These facilities and the optical diagnostics utilized to measure the respective data are described in this section.

2.1. Shock Tubes

For the CO laser absorption experiments, the Aerospace shock tube (AST) at Texas A&M University was utilized. The AST has a driven section with an inner diameter and length of 16.2 cm and 7.88 m, respectively. This pressure-driven shock tube utilizes 0.25 mm thick polycarbonate diaphragms to initiate shock propagation and generate pressures around 1.3 atm behind the reflected shock wave. To facilitate ideal and repeatable diaphragm rupture, a cross-shaped cutting blade is used downstream of the diaphragm. Five piezoelectric pressure transducers (PCB P113A22), over the last 2 m of the shock tube, were employed to detect shock passage and extrapolate the incident-shock velocity near the endwall. This velocity was then used to calculate the reflected-shock pressure and temperature to within an uncertainty of $\pm 1\%$ and $\pm 0.8\%$, respectively [21]. Pure helium was used as the driving gas, which, for the configuration and conditions, allowed for test times of up to 3 ms. Two sapphire windows at the sidewall location, 1.6 cm upstream from the endwall, were mounted transversely to allow laser access. Additionally, an RTV silicone-shielded pressure transducer (PCB P113A22) was located at the sidewall location to monitor pressure during the experiment. Since the main component of the mixtures in the driven section is argon and due to the low post-reflected-shock pressure (P_5), the

non-ideal boundary layer effects (i.e., dP^*/dt) were minimal [22,23]. Further details on the AST have been provided previously [24].

The heated, high-pressure shock tube (HPST) facility at Texas A&M University was utilized to measure the ignition delay times for DEC. The HPST's driven section has an inner diameter of 15.24 cm and is 5.03 m in length. In contrast to the AST, the HPST uses four pressure transducers (PCB 113B22) over the last 1.44 m of the shock tube to collect three incident-shock-velocity measurements to extrapolate the shock velocity as the wave reaches the endwall location. With these analogies in mind, similar pressure and temperature uncertainties were observed. In terms of IDT, this uncertainty in temperature translates to $\pm 20\%$ uncertainty for IDT [25]. Again, to generate 1 atm test pressures, 0.25 mm thick polycarbonate diaphragms paired with a downstream cutter were used. Using pure helium as the driver gas allowed for a maximum test time of 2.5 ms for the HPST. Note, however, that boundary-layer growth within shock tubes is exacerbated for real fuel–air mixtures [26]. The HPST was built with this in mind, utilizing a large inner diameter to minimize non-ideal effects, particularly the post-reflected-shock pressure rise (dP^*/dt), as the relative boundary-layer thickness is smaller for such geometries [27]. For the current study, custom-fit heating jackets were used to elevate the facility's initial temperature to 373 K. This temperature was chosen so the vapor pressure of DEC was at least four times that of the partial pressure in the HPST. Further details on the heating system and HPST can be found elsewhere [28].

Both shock tubes use systems of rotary vane pumps (Agilent DS 602 and DS 402) and turbomolecular pumps (Agilent Turbo V1001 Navigator) to achieve $<10^{-5}$ Torr prior to adding the test mixture to ensure mixture purity. Mixtures for the CO time history experiments in the AST were made manometrically in a 22.2 L mixing tank and highly diluted in helium and argon (79.25% argon and 20% helium), while mixtures for the IDT experiments in the HPST were made in a 55.6 L heated mixing tank (also heated to 373 K). Similar to the shock tube prior to experiments, the mixing tanks were evacuated to $<10^{-5}$ Torr using the vacuum system. A vial containing liquid DEC was connected to the gas handling manifold, then degassed several times to ensure only DEC was present within the vial. Component partial pressures when making mixtures were measured using capacitance manometers (MKS Baratron with 0–10 Torr, 0–100 Torr, and 0–1000 Torr ranges) and pressure transducers (Setra GCT-225 and ESI HI2300, 0–17 bar range). Each mixture was allowed to mix for at least an hour prior to use in the shock tube. A summary of the mixtures and conditions from the shock tube experiments in this study is presented in Table 1. Gases used for both shock tube and LFS experiments were obtained from Praxair with 99.999% purity and the fuel, obtained from Sigma-Aldrich, had an anhydrous purity of $\geq 99\%$.

Table 1. Summary of the mixtures and conditions investigated in the shock-tube experiments.

Mix	Mixture Composition (% mol.)				Conditions		
	DEC	O ₂	Diluent	ϕ	P ₅ (atm)	T ₅ (K)	Measured
1	0.0577%	0.6923%	79.25 Ar, 20% He	0.5	1.27 ± 0.06	1236–1669	CO abs.
2	0.1070%	0.6430%	79.25 Ar, 20% He	1.0	1.26 ± 0.1	1267–1574	CO abs.
3	0.1875%	0.5625%	79.25 Ar, 20% He	2.0	1.28 ± 0.08	1304–1638	CO abs.
4	1.720%	20.65%	Bal. N ₂	0.5	1.08 ± 0.08	1183–1403	OH* IDT
5	3.380%	20.30%	Bal. N ₂	1.0	1.15 ± 0.1	1191–1403	OH* IDT
6	6.545%	19.63%	Bal. N ₂	2.0	1.11 ± 0.13	1182–1406	OH* IDT

2.2. Optical Diagnostics

CO time histories were collected via transversely mounted window ports allowing access to the sidewall location, 1.6 cm upstream from the endwall of the AST. More detailed information on the CO laser diagnostic has been provided previously, but a brief description

is presented herein [29]. A quantum cascade laser producing coherent light near $4.8 \mu\text{m}$ allowed access to the $P(20) 1 \leftarrow 0$ transition band of CO at 2059.91 cm^{-1} . A separate cell containing a 10% CO, 90% Ar mixture was introduced into the beam's path to center the laser on this transition line prior to each experiment. Two detectors (InSb) were fitted with bandpass filters for collection of incident and transmitted light intensities, respectively. This band was relatively isolated from other potential absorbing species, most importantly from H_2O and CO_2 [30,31]. Experiments were conducted with the laser-light blocked to test broadband-emission detection of the detectors, and none was observed. Additionally, experiments were performed with the QCL tuned off-line, showing no interfering species during DEC combustion. Notably, these mixtures (1–3 in Table 1) were highly diluted to minimize the temperature change due to chemical reactions. Of this diluent, 20% was helium to accelerate the vibrational relaxation of CO [32]. Temperature predictions made by the TAMU model were used to account for temperature change during the experiment [33]. The high dilution was chosen to keep this temperature change below 100 K, minimizing any uncertainties from the temperature prediction of the model. Previous studies performed in similar conditions estimated the uncertainty in CO concentration to be within $\pm 3.8\%$ [34].

For the heated shock tube IDT experiments (mixtures 4–6 in Table 1), chemiluminescence of OH^* near 307 nm was observed at the sidewall and endwall locations of the shock tube using photomultiplier tubes (Hamamatsu 1P21) equipped with UV filters (307 nm center, 10 nm FWHM). Ignition delay time was then defined by the difference between the time of shock reflection and the linear extrapolation to zero emission of the steepest increase in OH^* emission at the endwall location. Significant pressure rise due to combustion was observed and can also be used to define ignition. Because of this, an endwall definition for IDT is appropriate, as the changing conditions during combustion artificially accelerate IDTs at the sidewall location [25,35]. Pressure traces at the sidewall and endwall locations as well as a OH^* trace from a representative experiment is given in Figure 2 to illustrate the IDT definition in the present study. Note that simultaneous sidewall and endwall pressure and OH^* emission are monitored, as this is imperative to ensuring homogeneous combustion is being observed [36,37].

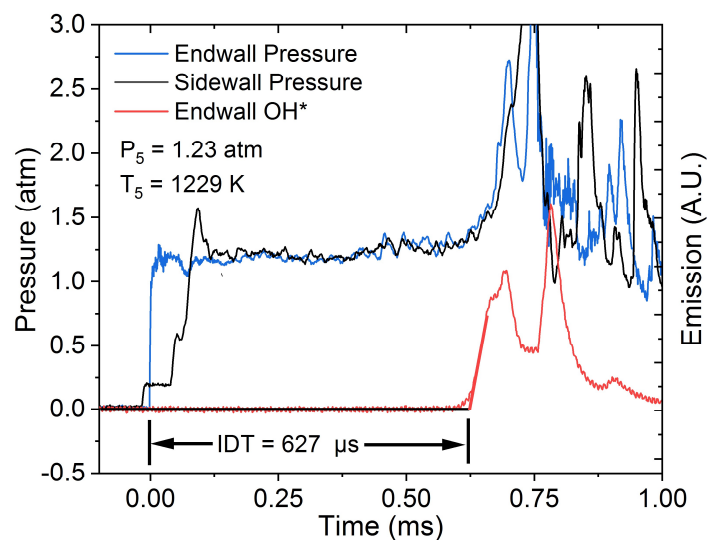


Figure 2. Representative pressure and OH^* emission time histories for an experiment at 1.23 atm and 1229 K for an equivalence ratio of $\phi = 2.0$ (Mix 6). Ignition delay time is defined as the difference between shock reflection at the endwall and the steepest initial rise in OH^* signal at the endwall.

2.3. Flame Speed Vessel

A heated, stainless steel, constant-volume vessel was used to collect LFS data in spherically expanding DEC flames. The 25.8 L cylindrical vessel had a 31.8 cm internal diameter and was 28 cm in length. Optical access in this vessel was available through two

opposing 12.7 cm diameter glass windows, which allowed for measurement of the LFS under near-constant pressure conditions. A more detailed description of the vessel can be found in Krejci et al. [38]. A custom-fit heating jacket, which can produce a uniform temperature of up to 600 K, was used to heat the vessel to avoid fuel condensation. For the present study, the initial temperature and pressure were 403 K and 1 atm, respectively. A Photron Fastcam SA1.1 camera with a rate of 10,000 fps was used in a Z-type schlieren imaging setup to capture the spherically propagating flame [39]. The collected images were then analyzed using an in-house Python code for edge detection, and the LFS was then calculated using the non-linear equation developed by Chen [40,41]. A known mass of fuel was introduced to the vessel via injection using a syringe, and the resulting partial pressure of fuel was then recorded using a 0–100 Torr pressure gauge. After complete evaporation of the fuel, the vessel was filled with synthetic air to the desired initial pressure (i.e., 1 atm). The final equivalence ratio was then reported based on the fuel partial pressure and the final total pressure. The resulting uncertainty in LFS using this experimental setup has been previously shown to be within $\pm 1\%$; however, for the current study, a conservative $\pm 5\%$ was adopted, which is similar to those under similar conditions for DEC in the literature [9,39].

2.4. Modeling

To assess the present study's mechanism and those from the literatures' ability to reproduce the CO time histories and IDT results presented herein, the closed homogeneous reactor in Chemkin 19.1 from Ansys was utilized [42]. Therein, the "Constrain Volume and Solve Energy Equation" assumption was used for the shock-tube experiments. As discussed, dP^*/dt was minimal and, therefore, was not included in modeling the experimental conditions. For LFS modeling, a one-dimensional laminar-flame simulation was performed using the Chemkin 19.1 package, using mixture averages transport and including the Soret effect [43]. To constrain the adaptive grid control parameter values, continuations were used, achieving between 1700 and 2000 grid points for each simulation [44].

As discussed, five modern chemical kinetics mechanisms have been developed to predict DEC pyrolysis and combustion; their details are summarized in Table 2. Note that Takahashi et al. and the TAMU models will be the main focus of this study, as they are both built on the developments of the older mechanisms. Recall that it was shown by Grégoire et al. [18] that the models of Nakamura et al. [8], Shahla et al. [9], Sun et al. [10], and even Takahashi et al. [15] are insufficient at reproducing CO time histories during fundamental DEC pyrolysis. The TAMU model is available as supplemental material in the study of Grégoire et al. [18].

Table 2. Characteristics of the five chemical kinetic models used for comparison with experiments.

Model	Numb. Species	Numb. Reactions	Year
Nakamura et al. [8]	355	1959	2015
Shahla et al. [9]	113	791	2017
Sun et al. [10]	341	1980	2017
Takahashi et al. [15]	370	2082	2022
Grégoire et al. [18] (TAMU)	231	1516	2023

3. Results

Seven data sets were taken for this study to investigate DEC combustion. These included six data sets collected in shock tubes, three using a CO laser absorption diagnostic to collect CO time histories, and three using a OH* chemiluminescence diagnostic to collect IDT data. The last data set utilized a constant-volume vessel to observe spherically expanding flames and collect laminar flame speeds. The results from these experiments, as well as predictions from chemical kinetics mechanisms, are presented in this section.

3.1. CO Time Histories

Experiments conducted under high dilution (79.25% Ar and 20% He) at fuel-lean (a–c), stoichiometric (d–f), and fuel-rich (g–i) cases are shown in Figure 3 for high-, mid-, and low-temperature conditions. As one can see, for the high- and medium-temperature cases for the fuel-lean and stoichiometric mixtures, a peak in the CO concentration was reached after a delay that increased when the temperature decreased. After this initial rapid formation of CO, the carbon monoxide concentration decreased with time due to the oxidation of CO into CO₂. On the other hand, for the fuel-rich case, the peak was not as well defined, and the CO reached a plateau level. This plateau was to be expected and is typically observed for mixtures when the oxygen concentration is insufficient to fully oxidize the fuel [19,34,45].

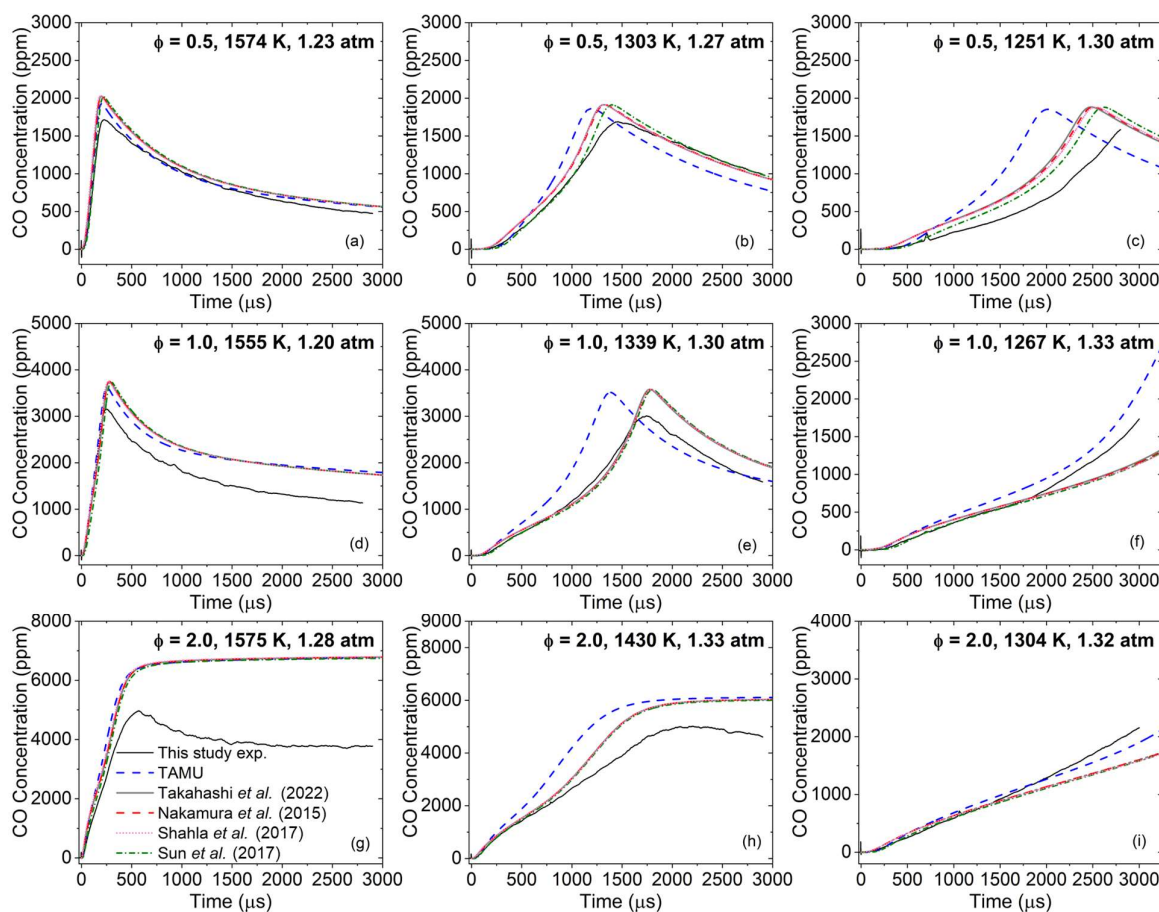


Figure 3. High-, mid-, and low-temperature traces (left to right) for $\phi = 0.5$ (a–c), 1.0 (d–f), and 2.0 cases (g–i, top to bottom). Modeling results are also shown for the mechanism from the present study (bold blue dashes), as well as those from Nakamura et al. [8] (red dashes), Sun et al. [10] (green dash-dots), Shahla et al. [9] (pink dots), and Takahashi et al. [15] (grey line).

Concerning the models, the shape of the profiles and experimental trends were well-captured by all models for the fuel-lean and stoichiometric cases. Little difference was seen between the models by Nakamura, Sun, and Takahashi; each basically builds on the earlier, but little change was observed for the CO concentration measurements. The CO concentration at the peak tended to be over-estimated by 10–15% by these models, and they also tend to be slightly over-reactive for the fuel-lean condition. At fuel-lean conditions, the Shahla model presented very similar predictions to those models, but was, however, in better agreement with the time-to-peak timing observed for the experiments at $\phi = 0.5$ (Figure 3b). Lastly, for the fuel-lean and stoichiometric mixtures, the TAMU model predicted lower levels of CO at the peak, in better agreement with the experimental

data, but this model was also more reactive, which induced a peak CO found earlier than the experimental one, notably at intermediate temperatures. For the fuel-rich case, the experimental profile at high temperature (Figure 3g) was not captured by the models, and the CO level at the plateau was significantly over-predicted by nearly 50%. At intermediate temperatures (Figure 3h), the shape was better predicted (at least during the timeframe of the experiment) and the TAMU model was still over-reactive (all the other models being extremely close in terms of predictions). However, at this condition, the difference between the models and the experimental profile was only 20–25% for the CO concentration. This result is rather surprising for the TAMU model, as it predicted a much smaller concentration of CO compared with the other models in pyrolysis conditions. Thus, the results of the present study seem to indicate the presence and preference of an alternative route for CO formation that uses the O₂ present in the mixture.

3.2. Ignition Delay Time

DEC ignition delay times collected near atmospheric pressure over a range of temperatures between 1182 and 1406 K behind reflected shock waves are shown in Figure 4 for (a) $\phi = 0.5$, (b) $\phi = 1.0$, and (c) $\phi = 2.0$. As can be seen, the evolution of the ignition delay time with the temperature followed the classical evolution observed for hydrocarbons at high temperatures. Models offered similar predictions (within a factor of two, typically) and predicted the experimental results with good accuracy overall and within the experimental uncertainty for the most part. The global activation energy (corresponding to the slope of the model) tended to be slightly higher for the model than what was observed experimentally. This larger activation energy leads to divergences between the models and the data below 1250 K for the (b) stoichiometric and (c) fuel-rich cases.

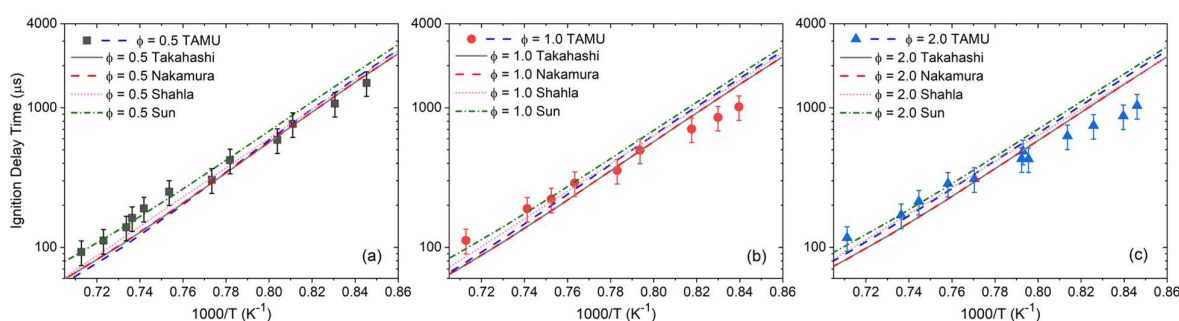


Figure 4. IDT for DEC/air mixtures at (a) $\phi = 0.5$, (b) $\phi = 1.0$, (c) $\phi = 2.0$, and comparison with model predictions (Nakamura et al. [8], Shahla et al. [9], Sun et al. [10], and Takahashi et al. [15]).

The comparison amongst all the equivalence ratios is visible in Figure 5, along with the predictions of the TAMU model. As one can see, there was a very small influence of the equivalence ratio on the ignition delay time. While the global activation energy (again, corresponding to the slope of the curve) seemed to slightly decrease as the equivalence ratio increased, as can be seen by comparing the extremes of the plots, it is worth pointing out that all the data for each equivalence ratio were within their experimental uncertainty for a given temperature. However, this decrease in the activation energy was also predicted by the model and translated to converging predictions toward the lowest temperatures of the range considered herein.

3.3. Laminar Flame Speed

The laminar flame speed results obtained during this study are visible in Figure 6, where the classical curve peaking at around $\phi = 1.1$ was obtained. The maximum laminar flame speed obtained experimentally was 55.6 cm/s at 403 K and 1 atm for the initial conditions. As one can see in Figure 6, the models considered herein were all within the experimental uncertainty (which appears large only because the y axis of the graph ranged between 40 and 60 cm/s), but they all fell under the experimental measurements. Among

these models, the TAMU, Shahla, and Nakamura models were the closest to the data. They also presented nearly identical predictions for stoichiometric and fuel-rich mixtures. At fuel-lean conditions, the Shahla model offered marginally better predictions.

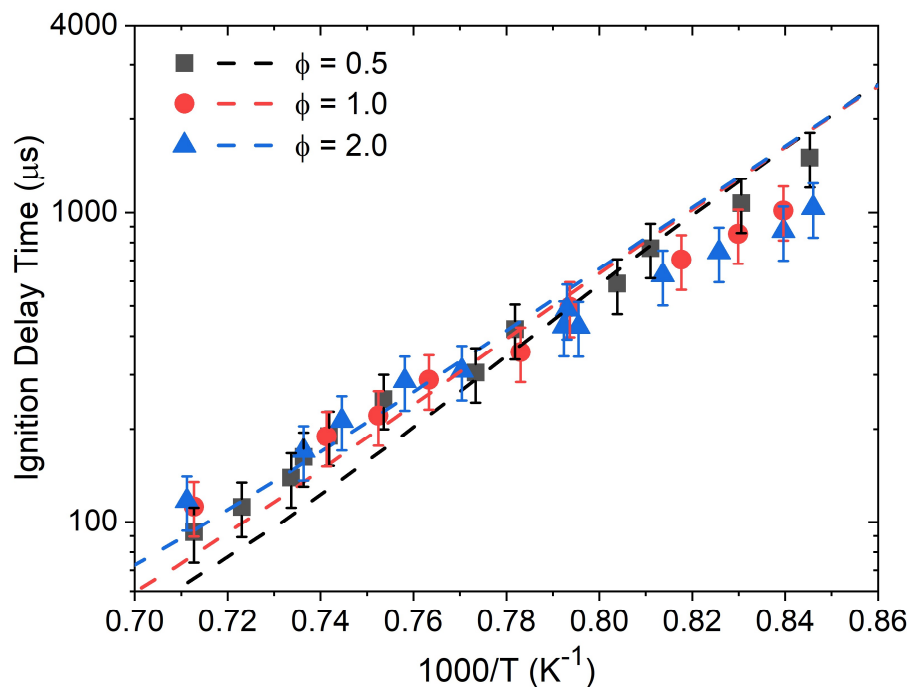


Figure 5. Ignition delay time results from this study compared with predictions from the model of the present study.

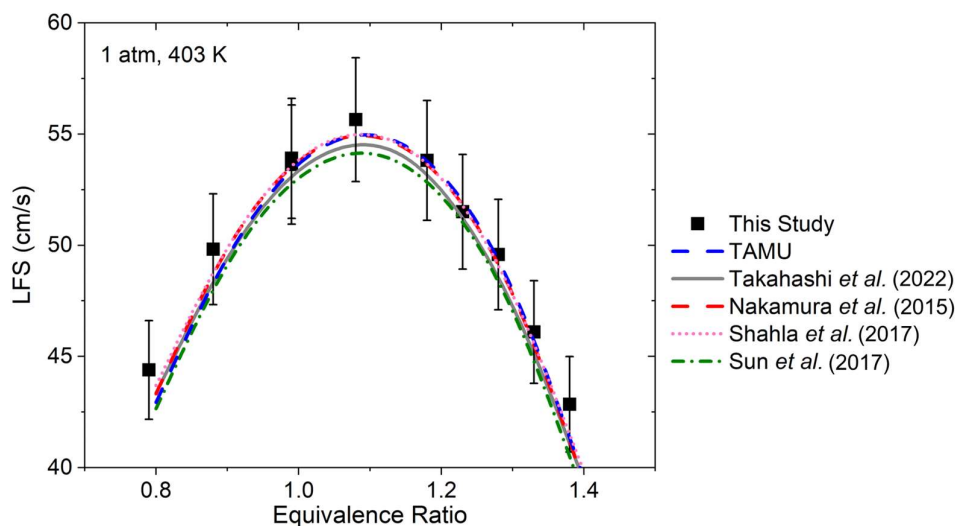


Figure 6. Laminar flame speed results from this study at initial conditions of 1 atm and 403 K compared with model predictions from the present study and those from the literature (Nakamura et al. [8], Shahla et al. [9], Sun et al. [10], and Takahashi et al. [15]).

The laminar flame speed obtained during this study can also be compared with data from the literature, namely Shahla et al. [8]. The results of this comparison are visible in Figure 7, where the dashed lines correspond to the predictions of the TAMU model. Note that, for the direct comparison at 1 atm, the data from this study had a slightly higher initial temperature (403 K) than that of Shahla et al. (393 K), owing to the slight difference in LFS at $\phi = 1.2$. As expected, the higher pressures presented lower LFS, and the TAMU model predicted these variations with accuracy over the entire range of conditions

investigated, except for the 2 atm, $\phi = 0.8$ data point, which also appeared higher than the experimental trend.

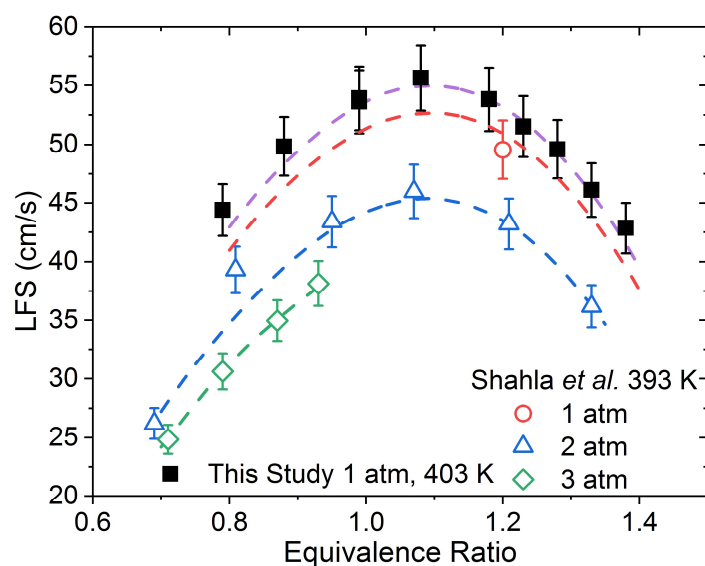


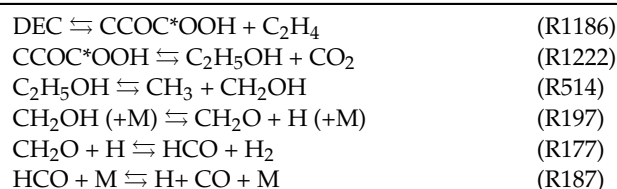
Figure 7. Laminar flame speed data from this study (solid square symbols) and that of Shahla et al. [8] (open symbols) compared with the TAMU model [15] (dashed purple line).

4. Discussion

As can be seen in Figures 4–7, global kinetics data such as ignition delay time and laminar flame speed were reproduced with high accuracy overall by the models considered herein. On the other hand, large discrepancies were observed for the CO profiles' predictions. This result illustrates the importance of this level of kinetics data, where the high dilution level translates to minor changes in pressure and temperature during the course of the experiment, and where the profile of the species followed experimentally typically depends on a limited set of reactions and the accuracy of their reaction coefficients. This discrepancy in the models' performance between global kinetics data and kinetics measurements has been observed recently in the authors' work on various alcohols [25,36,46]. In the authors' opinion, since the global kinetics data are accurately reproduced, the CO profiles presented herein should be the main focus of this discussion section to provide ways to improve the model.

To this end, it is interesting to first compare the performance of the models considered herein on CO profiles obtained during the pyrolysis of DEC [18], shown in Figure 8. As can be seen, (i) all models but the TAMU one largely over-estimated the amount of CO produced, and (ii) the TAMU model was very slightly less reactive than the other models concerning the rate at which the CO level reached a plateau. With these observations in mind, it is interesting to see in Figure 3 that the TAMU model is now notably more reactive than the other models and reached the same amount of CO at $\phi = 2.0$ than the other models, which is the condition the closest to the pyrolysis condition investigated in [18] and visible in Figure 8.

Under pyrolysis conditions, as seen in the authors' previous study, the CO formation from DEC pyrolysis occurs primarily via (the reaction numbers and the names of the molecules and radicals correspond to those in the TAMU model):



This pathway is denominated Pathway A. However, note that there is a secondary pathway after the two first decomposition reactions:

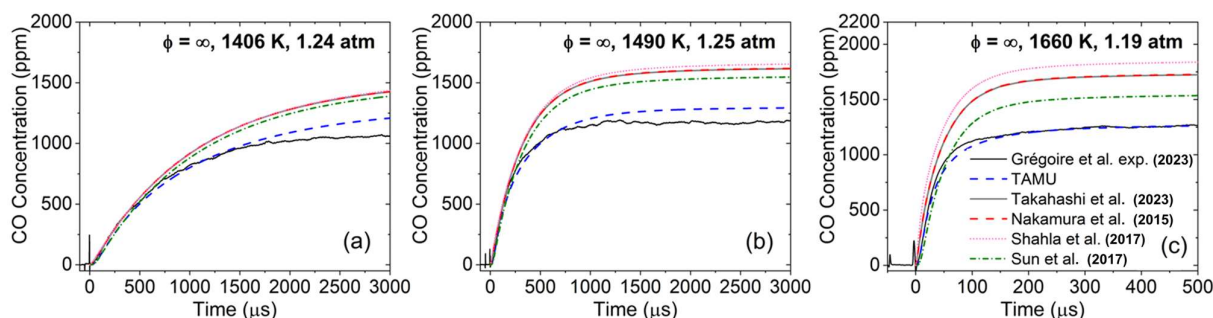
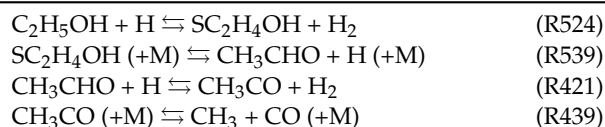


Figure 8. CO time histories for (a) low-, (b) mid-, and (c) high-temperature cases during DEC pyrolysis from Grégoire et al. [18] compared with the models by TAMU [18] and those from the literature. Mixture is 0.0025 DEC, 0.2 He, 0.7975 Ar (models are (Nakamura et al. [8], Shahla et al. [9], Sun et al. [10], and Takahashi et al. [15])).

As can be concluded from this reaction pathway analysis, under pyrolysis conditions, ethanol pyrolysis is chiefly responsible for the formation of CO during DEC pyrolysis. One can also see that the main reaction pathway produces two C_2H_4 molecules (in addition to ethanol and CO_2) from one DEC molecule. This finding is also visible in Figure 9a, where the CO concentration increased as ethanol was depleted, whereas the concentration of C_2H_4 remained nearly constant after rapidly reaching a plateau.

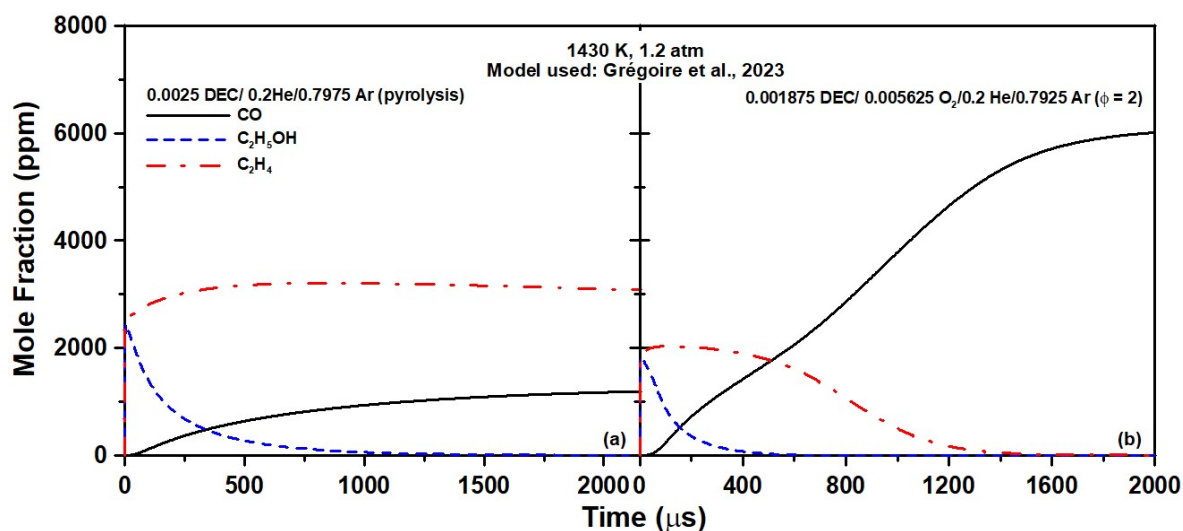


Figure 9. Computed CO, C_2H_5OH , and C_2H_4 profiles from (a) DEC pyrolysis and (b) DEC oxidation at $\phi = 2.0$ (dilution in He and Ar corresponding to the experiments listed in Table 1) at 1430 K and 1.2 atm. Model used: Grégoire et al. [18].

Focusing on ethanol pyrolysis, recent work from the authors [29] showed that CO formation from ethanol pyrolysis is also largely over-estimated by base models, which directly translates to over-predictions of CO levels during DEC pyrolysis [18]. The over-prediction of the CO concentration during ethanol pyrolysis is also observed for the DEC

models from the literature considered herein, as can be seen in Figure 10. As one can see, at low temperatures (Figure 10a), the TAMU model was more reactive and produced slightly more CO than the other DEC models. However, at high temperatures (Figure 10b), the TAMU model was the only one in close agreement (within the experimental uncertainty) with the data, while all other models had nearly identical predictions and largely over-predicted the CO concentration. The model from Saggese et al. [47] was also tested over these conditions to assess the performance of a recent model dedicated to alcohols on the CO profile predictions. As one can see, this model was the most over-reactive and over-predicting of the ones tested. This result further reinforces the assessment made by the authors that ethanol [18,29] and methanol [18] chemistries need to be revisited, preferentially using this type of spectroscopic measurements over global kinetics data. Interestingly, starting with 2500 ppm of DEC (Figure 8) or 2500 ppm of ethanol (Figure 10) produced about the same amount of CO when the plateau was reached (i.e., about 1150 ppm), demonstrating the predominance of the ethanol pathway during the pyrolysis of DEC. Note that removing the updates in the ethanol chemistry adopted in the authors' former study [18] allowed us to only partly reduce the over-reactivity observed during DEC oxidation (but did bring the CO level up to what was observed for the other models for ethanol and DEC pyrolysis).

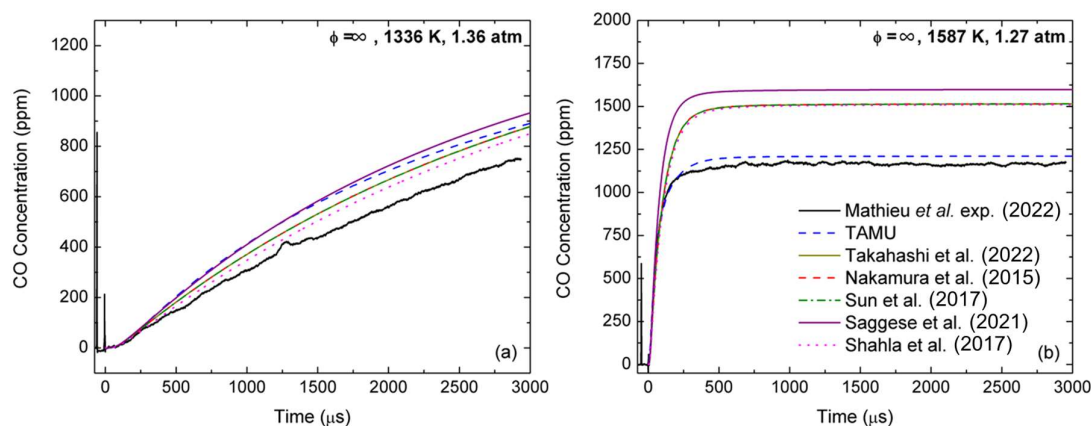
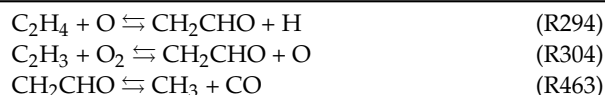


Figure 10. CO profiles from ethanol pyrolysis from Mathieu et al. [29] at (a) 1336 K, 1.36 atm, and (b) 1587 K, 1.27 atm, and comparison with DEC models from the literature (models are (Nakamura et al. [8], Shahla et al. [9], Sun et al. [10], Takahashi et al. [15], and Saggese et al. [47])).

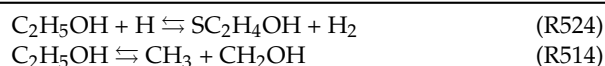
The fact that the CO formation during DEC oxidation was the same for all models for fuel-rich conditions (Figure 3g–i), despite the results from Figures 8 and 10 obtained in pyrolysis exhibiting large differences, shows that the ethanol pyrolysis pathway is not necessarily predominant in the presence of oxygen with regard to CO production and, most likely, additional reaction pathways are involved. This behavior is visible in Figure 9b, where the ethanol was depleted far before the CO level reached its plateau. According to this figure and the visible inflexion in the CO profile coinciding with the start of the C_2H_4 oxidation, it would appear as if the CO formation from ethanol occurs and almost finishes before the CO formation from C_2H_4 starts. To investigate this issue, a numerical analysis was conducted with the TAMU model. This model was selected because, despite providing the least accurate predictions at $\phi = 2.0$, for example, it has a stronger foundation when it comes to ethanol and DEC pyrolysis. To understand the CO formation process better during DEC oxidation, the case at $\phi = 2.0$, 1430 K (Figure 3h) was selected. For this specific case, most of the timeframe of the experiment was dedicated to CO formation, which allowed investigating and decoupling of the reaction pathways involved at various times. At this temperature, DEC was practically consumed within less than 4 μs , and within the first 5 μs DEC went on to form ethanol and CO via the ethanol pyrolysis pathway, as described earlier (R1186–R187). Note that a maximum of 1830 ppm of ethanol was predicted

by the model for an initial DEC concentration of 1875 ppm, demonstrating the large initial importance of this pathway (despite ethanol preferably producing C_2H_4 via dehydration, $C_2H_5OH \rightleftharpoons C_2H_4 + H_2O$ (R593)). However, in the presence of oxygen, another pathway also produces CO:

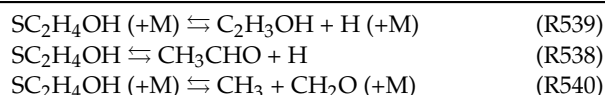


Note that CH_2CO can also isomerize into acetyl radical (CH_3CO) via oxiranyl (C_2H_3O1-2): $CH_2CHO \rightleftharpoons C_2H_3O1-2 \rightleftharpoons CH_3CO$ and then form CO via $CH_3CO (+M) \rightleftharpoons CH_3 + CO (+M)$ (R439). This pathway is denominated Pathway B.

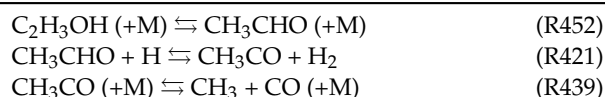
At only 20 μs , CO is still largely produced via the ethanol pyrolysis sequence R1186-R187 (Pathway A), although ethanol still mostly undergoes dehydration to produce C_2H_4 via R593. However, reactions with H radicals and other thermal decomposition pathways become important and lead to another CO formation pathway (Pathway C) via:



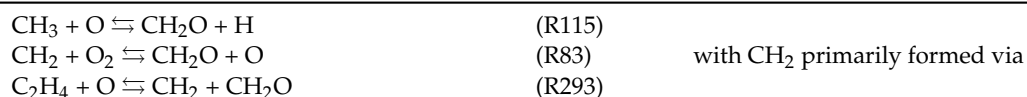
with CH_2OH forming CO via the sequence R197 \rightarrow R177 \rightarrow R187 described above and SC_2H_4OH forming CO via:



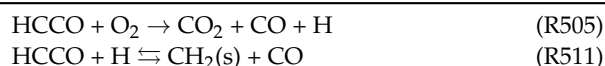
with CH_2O going to CO via R177 \rightarrow R187 and $CH_2O + H \rightleftharpoons H + CO + H_2$ (R186)). This is followed by:



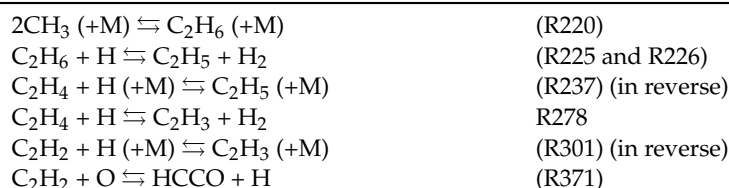
In parallel to this CO formation from ethanol (Pathways A and C), C_2H_4 also produces CO via Pathway B. This chemistry continues until ethanol is fully consumed at around 500 μs . However, as the concentration of ethanol decreases rapidly, other pathways start producing CH_2O (and, thus, CO via HCO) via the remaining C_2H_4 produced from R1186 and R593 and CH_3 produced via R439, R514, and R540:



At around 500 μs , another pathway (Pathway D) starts appearing:



with HCCO coming from



Past the 500 μs mark, at the specific condition of Figure 3h, CO mostly forms from these CH_3 -based pathways directly from CH_3 or from $\text{C}_2\text{H}_6 \rightarrow \text{HCCO}$ after the recombination of methyl radicals. As one can see from this analysis, the CO formation from DEC oxidation has a much richer chemistry than that of DEC pyrolysis. Since the formation of CO during DEC/ethanol pyrolysis is well-captured under the present conditions, it can be concluded that the large over-estimation of the CO level by the models is due to the oxidation chemistry of C_2H_4 (while some reactions involving ethanol cannot be excluded given that oxidative conditions have not been tested experimentally). This is confirmed by the sensitivity and rate of production (ROP) analyses conducted for the case selected and visible in Figure 11. As can be seen for the sensitivity analysis (Figure 11a), the DEC decomposition stages leading to $\text{C}_2\text{H}_5\text{OH}$ (R1186 followed by R1222) were important at the very beginning of the experiment (this is difficult to see, as they are along the y axis, and so is R1251, the only reaction common to the sensitivity and ROP analysis). Beside the classical branching reaction R11, the reaction R514 involved in Pathway A had a very large promoting importance during the first millisecond. As the sensitivity of R514 decreased, one can note the growing inhibiting influence of R58 ($\text{CH}_3 + \text{H} (+\text{M}) \rightleftharpoons \text{CH}_4 (+\text{M})$) peaking at around 1000 μs . This reaction was inhibiting, since it consumed the methyl radicals that were at the base of the CH_3 pathways for CO described above.

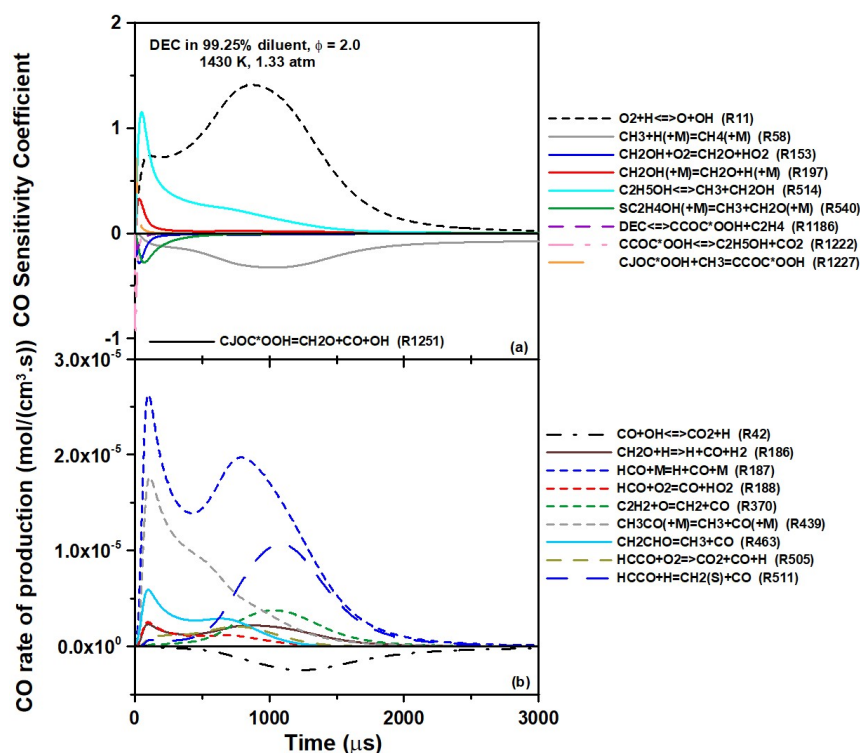


Figure 11. (a) CO sensitivity and (b) rate of production analyses for a mixture of DEC at $\phi = 2.0$ in 99.25% dilution, 1430 K, and 1.33 atm.

Concerning the ROP analysis, the dominant role of R187 is visible. Note the two production peaks of CO for this reaction, with the ethanol and CH_3 as the original source of HCO for the first and second peak, respectively. One can also see the importance of R439 coming from ethanol (Pathway C) during the first 500 μs and the importance of reactions with C_2H_2 (R370) and HCCO (R505 and R511), peaking around 1000 μs and representing the CO formation Pathway D. Given that the CO production from ethanol pyrolysis can be reproduced with good accuracy overall, the authors believe that the CO formation from Pathway D, involving species in C2 (C_2H_6 , C_2H_4 , C_2H_2 , and HCCO), is the main factor responsible for the over-prediction of CO by the models. Since C_2H_4 is present in large concentrations in this system, as it is also produced by the DEC decomposition

steps leading to ethanol, it would be a good first candidate for a subsequent study on CO formation. To the best of the authors' knowledge, there is no study in a shock tube where the CO formation from C₂H₄ oxidation was measured. Additionally, these C₂ species are part of the "base mechanism" common to most hydrocarbons. Thus, the authors do not believe that changing the rate coefficients of a few reactions involving C₂ species to better fit the results of this study would be appropriate, as the base chemistry on the models used herein has been extensively validated and any change in this area would require extensive validation, as it might otherwise deteriorate the predictions for many other fuels in various conditions.

Lastly, a sensitivity analysis was conducted with the Grégoire et al. model for OH* for the conditions used to investigate the ignition delay time (conditions set at 1275 K and 1.1 atm for all equivalence ratios). Results from this analysis are visible in Figure 12. In this figure, note that R1186 (DEC \rightleftharpoons CCOC*OOH + C₂H₄) is not in the top ten reactions for the fuel-lean mixture, whereas the sensitivity is by far the largest for the stoichiometric and fuel-rich cases. In fact, the sensitivity coefficient for R1186 was divided by a factor of seven at $\phi = 1.0$ and nine at $\phi = 2.0$, so the other reactions could still be visible when normalizing the data. Additionally, the sensitivity to R1186 occurred within the first few microseconds only, whereas all the other reactions displayed their sensitivity to OH* at the ignition event. For $\phi = 0.5$, the classical branching reaction R10 (O₂ + H \rightleftharpoons OH + O) was the most sensitive reaction, and this reaction was also the most promoting reaction for the other conditions. R122 (CH₃ + HO₂ \rightleftharpoons CH₃O + OH), R279 (C₂H₄ + OH \rightleftharpoons C₂H₃ + H₂O), and R27 (H₂O₂ (+M) \rightleftharpoons OH + OH (+M)) were also promoting reactions in all cases, and it is worth mentioning that their sensitivities increased with the equivalence ratio. It is interesting to see that several sensitive reactions involved HO₂ chemistry, which is typically not so prominent at high-temperature/low-pressure conditions. This importance of HO₂ chemistry was due to the prominence of ethanol chemistry, as described above and visible in Figure 12, which led to the production of HO₂ via reactions like that of R545 (SC₂H₄OH + O₂ \rightleftharpoons CH₃CHO + HO₂). HO₂ also played an important role in the terminating reaction R65 (CH₃ + HO₂ \rightleftharpoons CH₄ + O₂), which largely inhibited the reactivity. In addition to R1186, the most inhibiting reaction for all cases was R524 (C₂H₅OH + H \rightleftharpoons SC₂H₄OH + H₂), which competed with R10. The sensitivities of R65 and R525 also increased with equivalence ratio.

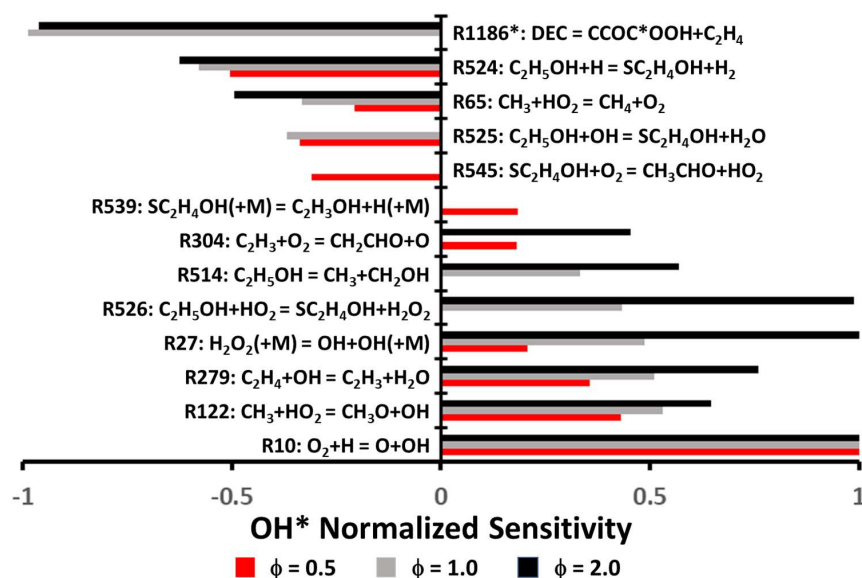


Figure 12. OH* normalized sensitivity analysis for the top ten reactions with the model of Grégoire et al. [18]. Conditions: 1275 K, 1.1 atm for DEC air mixture at $\phi = 0.5, 1.0,$ and 2.0 . R1186*: the sensitivity was divided by a factor 7 and 9 for $\phi = 1.0$ and 2.0 , respectively, for the sake of readability.

5. Conclusions

The combustion chemistry of DEC was investigated experimentally by measuring a large variety of combustion parameters such as ignition delay times, laminar flame speeds, and CO time histories over a wide range of conditions and near atmospheric pressures. These results were compared with detailed kinetics models from the literature, and this comparison shows that the global kinetics data (ignition delay times and laminar flame speeds) are accurately predicted by all of the models considered. On the other hand, the kinetics measurement of CO showed significant room for improvement in the models. A numerical analysis was conducted and this analysis exhibited complex chemistry, with several pathways involved at different times. It is likely that the CO formation from species in C2, notably C₂H₄, as described in the models is the reason behind the inaccurate predictions during DEC combustion (although C₂H₅OH oxidation cannot be fully excluded). The authors believe that a complementary shock tube laser-absorption-based study of the CO formation during C₂H₄ oxidation would be necessary to clarify and possibly solve this issue.

Author Contributions: Article writing: S.P.C., C.M.G., Y.M.A., and O.M., data acquisition: S.P.C., C.M.G., and Y.M.A., funding acquisition: O.M., Writing—review and Editing: E.L.P. All authors have read and agreed to the published version of the manuscript.

Funding: The authors would like to thank the National Science Foundation for the financial support of this study (award # 2037795). Additional support came from the TEES Turbomachinery Laboratory through a Ralph-James Fellowship for C.M.G. and S.P.C. as well as from King Saud University (KSU) through Saudi Arabian Cultural Mission (SACM) fellowship# 4/52/60746 for Y.M.A.

Data Availability Statement: The data presented in the article are available upon request to the corresponding author.

Conflicts of Interest: The authors declare no conflict of interest.

References

1. Wang, Q.; Ping, P.; Zhao, X.; Chu, G.; Sun, J.; Chen, C. Thermal runaway caused fire and explosion of lithium ion battery. *J. Power Sources* **2012**, *208*, 210–224.
2. Harris, S.J.; Timmons, A.; Pitz, W.J. A combustion chemistry analysis of carbonate solvents used in Li-ion batteries. *J. Power Sources* **2009**, *193*, 855–858.
3. Larsson, F.; Andersson, P.; Blomqvist, P.; Mellander, B.-E. Toxic fluoride gas emissions from lithium-ion battery fires. *Sci. Rep.* **2017**, *7*, 10018.
4. Li, Q.; Chen, J.; Fan, L.; Kong, X.; Lu, Y. Progress in electrolytes for rechargeable Li-based batteries and beyond. *Green Energy Environ.* **2016**, *1*, 18–42.
5. Aguado-Deblas, L.; Hidalgo-Carrillo, J.; Bautista, F.M.; Luna, C.; Calero, J.; Posadillo, A.; Romero, A.A.; Luna, D.; Estévez, R. Biofuels from diethyl carbonate and vegetable oils for use in triple blends with diesel fuel: Effect on performance and smoke emissions of a Diesel engine. *Energies* **2020**, *13*, 6584.
6. Kozak, M.; Merksiz, J.; Bielaczyc, P.; Szczotka, A. *The Influence of Oxygenated Diesel Fuels on a Diesel Vehicle PM/NO_x Emission Trade-Off*; Report No. 0148-7191; SAE Technical Paper; SAE International: Warrendale, PA, USA, 2009.
7. Pacheco, M.A.; Marshall, C.L. Review of dimethyl carbonate (DMC) manufacture and its characteristics as a fuel additive. *Energy Fuels* **1997**, *11*, 2–29.
8. Nakamura, H.; Curran, H.J.; Córdoba, A.P.; Pitz, W.J.; Dagaut, P.; Togbé, C.; Sarathy, S.M.; Mehl, M.; Agudelo, J.R.; Bustamante, F. An experimental and modeling study of diethyl carbonate oxidation. *Combust. Flame* **2015**, *162*, 1395–1405.
9. Shahla, R.; Togbé, C.; Thion, S.; Timothée, R.; Lailliau, M.; Halter, F.; Chauveau, C.; Dayma, G.; Dagaut, P. Burning velocities and jet-stirred reactor oxidation of diethyl carbonate. *Proc. Combust. Inst.* **2017**, *36*, 553–560.
10. Sun, W.; Huang, C.; Tao, T.; Zhang, F.; Li, W.; Hansen, N.; Yang, B. Exploring the high-temperature kinetics of diethyl carbonate (DEC) under pyrolysis and flame conditions. *Combust. Flame* **2017**, *181*, 71–81.
11. AlAbbad, M.; Giri, B.R.; Szori, M.; Viskolcz, B.; Farooq, A. A high temperature kinetic study for the thermal unimolecular decomposition of diethyl carbonate, *Chem. Phys. Lett.* **2017**, *684*, 390–396.
12. Herzler, J.; Manion, J.A.; Tsang, W. Single-Pulse Shock Tube Studies of the Decomposition of Ethoxy Compounds. *J. Phys. Chem. A* **1997**, *101*, 5494–5499.
13. Sela, P.; Zhang, Y.; Herzler, J.; Fikri, M.; Schulz, C.; Peukert, S. Pyrolysis of diethyl carbonate: Shock-tube and flow-reactor measurements and modeling. *Proc. Combust. Inst.* **2021**, *38*, 987–996.

14. Kanayama, K.; Takahashi, S.; Morikura, S.; Nakamura, H.; Tezuka, T.; Maruta, K. Study on oxidation and pyrolysis of carbonate esters using a micro flow reactor with a controlled temperature profile. Part I: Reactivities of dimethyl carbonate, ethyl methyl carbonate and diethyl carbonate. *Combust. Flame* **2022**, *237*, 111810.
15. Takahashi, S.; Kanayama, K.; Morikura, S.; Nakamura, H.; Tezuka, T.; Maruta, K. Study on oxidation and pyrolysis of carbonate esters using a micro flow reactor with a controlled temperature profile. Part II: Chemical kinetic modeling of ethyl methyl carbonate. *Combust. Flame* **2022**, *238*, 111878.
16. Mathieu, O.; Grégoire, C.M.; Turner, M.A.; Mohr, D.J.; Alturaifi, S.A.; Thomas, J.C.; Petersen, E.L. Experimental Investigation of the Combustion Properties of an Average Thermal Runaway Gas Mixture from Li-Ion Batteries. *Energy Fuels* **2022**, *36*, 3247–3258.
17. Baigmohammadi, M.; Patel, V.; Martinez, S.; Panigrahy, S.; Ramalingam, A.; Burke, U.; Somers, K.P.; Heufer, K.A.; Pekalski, A.; Curran, H.J. A comprehensive experimental and simulation study of ignition delay time characteristics of single fuel C1–C2 hydrocarbons over a wide range of temperatures, pressures, equivalence ratios, and dilutions. *Energy Fuels* **2020**, *34*, 3755–3771.
18. Grégoire, C.M.; Cooper, S.P.; Khan-Ghauri, M.; Alturaifi, S.A.; Petersen, E.L.; Mathieu, O. Pyrolysis Study of Dimethyl Carbonate, Diethyl Carbonate, and Ethyl Methyl Carbonate using Shock-Tube Spectroscopic CO Measurements and Chemical Kinetics Investigation. *Combust. Flame* **2023**, *249*, 112594.
19. Atherley, T.; de Persis, S.; Chaumeix, N.; Fernandes, Y.; Bry, A.; Comandini, A.; Mathieu, O.; Alturaifi, S.; Mulvihill, C.; Petersen, E. Laminar flame speed and shock-tube multi-species laser absorption measurements of Dimethyl Carbonate oxidation and pyrolysis near 1 atm. *Proc. Combust. Inst.* **2021**, *38*, 977–985.
20. Mathieu, O.; Diévar, P.; Turner, M.; Mohr, D.; Grégoire, C.; Alturaifi, S.; Catoire, L.; Petersen, E. Experimental and detailed kinetics modeling study of the fire suppressant properties of di (2,2,2trifluoroethyl) carbonate. *Proc. Combust. Inst.* **2023**; *in press*.
21. Petersen, E.L.; Rickard, M.J.; Crofton, M.W.; Abbey, E.D.; Traum, M.J.; Kalitan, D.M. A Facility for Gas-and Condensed-Phase Measurements behind Shock Waves. *Meas. Sci. Technol.* **2005**, *16*, 1716.
22. Lipkowicz, J.T.; Nativel, D.; Cooper, S.P.; Wlokas, I.; Fikri, M.; Petersen, E.L.; Schulz, C.; Kempf, A.M. Numerical Investigation of Remote Ignition in Shock Tubes. *Flow Turbul. Combust.* **2021**, *106*, 471–498.
23. Mulvihill, C.R.; Alturaifi, S.A.; Petersen, E.L. A shock-tube study of the $N_2O + M \rightleftharpoons N_2 + O + M$ ($M = Ar$) rate constant using N_2O laser absorption near 4.6 μm . *Combust. Flame* **2021**, *224*, 6–13.
24. Grégoire, C.M.; Westbrook, C.K.; Kukkadapu, G.; Cooper, S.P.; Alturaifi, S.A.; Mathieu, O.; Petersen, E.L. Shock-tube spectroscopic CO and H_2O measurements during 2-methyl-1-butene combustion and chemical kinetics modeling. *Combust. Flame* **2022**, *238*, 111919.
25. Cooper, S.P.; Grégoire, C.M.; Mohr, D.J.; Mathieu, O.; Alturaifi, S.A.; Petersen, E.L. An Experimental Kinetics Study of Isopropanol Pyrolysis and Oxidation behind Reflected Shock Waves. *Energies* **2021**, *14*, 6808.
26. Hargis, J.W.; Petersen, E.L. Shock-tube boundary-layer effects on reflected-shock conditions with and without CO_2 . *AIAA J.* **2017**, *55*, 902–912.
27. Nativel, D.; Cooper, S.P.; Lipkowicz, T.; Fikri, M.; Petersen, E.L.; Schulz, C. Impact of shock-tube facility-dependent effects on incident-and reflected-shock conditions over a wide range of pressures and Mach numbers. *Combust. Flame* **2020**, *217*, 200–211.
28. Cooper, S.P.; Mathieu, O.; Schoegl, I.; Petersen, E.L. High-pressure ignition delay time measurements of a four-component gasoline surrogate and its high-level blends with ethanol and methyl acetate. *Fuel* **2020**, *275*, 118016.
29. Mathieu, O.; Grégoire, C.M.; Khan-Ghauri, M.; Cooper, S.P.; Petersen, E.L. Experimental study of the formation of CO during ethanol pyrolysis and dry reforming with CO_2 . *Appl. Energy Combust. Sci.* **2022**, *11*, 100076.
30. He, D.; Shi, L.; Nativel, D.; Herzler, J.; Fikri, M.; Schulz, C. CO-concentration and temperature measurements in reacting CH_4/O_2 mixtures doped with diethyl ether behind reflected shock waves. *Combust. Flame* **2020**, *216*, 194–205.
31. Spearrin, R.; Goldenstein, C.; Jeffries, J.; Hanson, R. Quantum cascade laser absorption sensor for carbon monoxide in high-pressure gases using wavelength modulation spectroscopy. *Appl. Opt.* **2014**, *53*, 1938–1946.
32. He, D.; Nativel, D.; Herzler, J.; Jeffries, J.B.; Fikri, M.; Schulz, C. Laser-based CO concentration and temperature measurements in high-pressure shock-tube studies of n-heptane partial oxidation. *Appl. Phys. B* **2020**, *126*, 142.
33. Mulvihill, C.; Petersen, E. High-temperature argon broadening of CO_2 near 2190 cm^{-1} in a shock tube. *Appl. Phys. B* **2017**, *123*, 255.
34. Mathieu, O.; Mulvihill, C.R.; Petersen, E.L. Assessment of modern detailed kinetics mechanisms to predict CO formation from methane combustion using shock-tube laser-absorption measurements. *Fuel* **2019**, *236*, 1164–1180.
35. Petersen, E.L. Interpreting Endwall and Sidewall Measurements in Shock-Tube Ignition Studies. *Combust. Sci. Technol.* **2009**, *181*, 1123–1144.
36. Mathieu, O.; Pinzón, L.T.; Atherley, T.M.; Mulvihill, C.R.; Schoel, I.; Petersen, E.L. Experimental study of ethanol oxidation behind reflected shock waves: Ignition delay time and H_2O laser-absorption measurements. *Combust. Flame* **2019**, *208*, 313–326.
37. Cooper, S.P.; Mathieu, O.; Mohr, D.J.; Petersen, E.L. Ignition Chemistry of Syngas Highly Diluted in CO_2 . In Proceedings of the ASME Turbo Expo 2022, Rotterdam, The Netherlands, 13–17 June 2022.
38. Krejci, M.C.; Mathieu, O.; Vissotski, A.J.; Ravi, S.; Sikes, T.G.; Petersen, E.L.; Kérmonès, A.; Metcalfe, W.; Curran, H.J. Laminar Flame Speed and Ignition Delay Time Data for the Kinetic Modeling of Hydrogen and Syngas Fuel Blends. *J. Eng. Gas Turbines Power* **2013**, *135*, 021503.
39. Sikes, T.; Mannan, M.S.; Petersen, E.L. An experimental study: Laminar flame speed sensitivity from spherical flames in stoichiometric CH_4 -air mixtures. *Combust. Sci. Technol.* **2018**, *190*, 1594–1613.

40. Chen, Z. On the extraction of laminar flame speed and Markstein length from outwardly propagating spherical flames. *Combust. Flame* **2011**, *158*, 291–300.
41. Turner, M.A.; Paschal, T.T.; Parajuli, P.; Kulatilaka, W.D.; Petersen, E.L. Application of high-speed, species-specific chemiluminescence imaging for laminar flame speed and Markstein length measurements in spherically expanding flames. *Exp. Therm. Fluid Sci.* **2021**, *129*, 110477.
42. ANSYS. *ChemKin 19.1*; ANSYS: San Diego, CA, USA, 2018.
43. Turner, M.A.; Paschal, T.T.; Parajuli, P.; Kulatilaka, W.D.; Petersen, E.L. Resolving flame thickness using high-speed chemiluminescence imaging of OH* and CH* in spherically expanding methane–air flames. *Proc. Combust. Inst.* **2021**, *38*, 2101–2108.
44. Turner, M.; Petersen, E. High-Pressure Laminar Flame Speeds and Markstein Lengths of Syngas Flames Diluted in Carbon Dioxide and Helium. *J. Eng. Gas Turbines Power* **2023**, *145*, 021022.
45. Mathieu, O.; Cooper, S.P.; Alturaifi, S.; Mulvihill, C.R.; Atherley, T.M.; Petersen, E.L. Shock-Tube Laser Absorption Measurements of CO and H₂O during Iso-Octane Combustion. *Energy Fuels* **2020**, *34*, 7533–7544.
46. Pinzón, L.T.; Mulvihill, C.R.; Schoegl, I.M.; Petersen, E.L. Ignition Delay Time and H₂O Measurements During Methanol Oxidation Behind Reflected Shock Waves. *Combust. Flame* **2019**, *203*, 143–156.
47. Saggese, C.; Thomas, C.M.; Wagnon, S.W.; Kukkadapu, G.; Cheng, S.; Kang, D.; Goldsborough, S.S.; Pitz, W.J. An improved detailed chemical kinetic model for C3-C4 linear and iso-alcohols and their blends with gasoline at engine-relevant conditions. *Proc. Combust. Inst.* **2021**, *38*, 415–423.

Disclaimer/Publisher’s Note: The statements, opinions and data contained in all publications are solely those of the individual author(s) and contributor(s) and not of MDPI and/or the editor(s). MDPI and/or the editor(s) disclaim responsibility for any injury to people or property resulting from any ideas, methods, instructions or products referred to in the content.